This is the author accepted manuscript.

Optimising Tibia Implants: Comparative Study of Lattice Designs and Material Performance under Gait Cycles

Meysam Nasr Azadani[1,3], Nandhu Narayanan[1], Karthikeyan Ramachandran[2*] and Constance L Gnanasagaran[2]

[1]School of Mechanical, Aerospace and Automotive Engineering, Coventry University, Priory Place, Coventry CV1 5FB, United Kingdom.
[2]School of Engineering and the Environment, Kingston University, Roehampton Vale Campus, London SW15 3DW, United Kingdom.
[3]School of Engineering and Sustainable Development, De Montfort University, The Gateway, Leicester, United Kingdom, LE1 9BH.

Abstract

This study advances orthopaedic implant design by examining the impact of lattice structures on gait cycles and integrating biomimicry principles for superior patient outcomes. Using Finite Element Analysis (FEA), three lattice designs; Face Centred Cubic (FCC), Body Centred Cubic (BCC), and a hybrid Face-Body Centred Cubic (FBCC) were evaluated with materials including Ni-Ti Shape Memory Alloy, TNTZ Alloy, and AZ91D Alloy. AZ91D emerged as the optimal material, offering the best balance of strength and weight. Tibia bone implants made from AZ91D were tested under various gait cycle conditions, including loading-level knee bending, 20% bending, and 30% bending, where the FBCC structure outperformed others due to its enhanced load transfer capabilities. Porosity effects were analysed by varying strut diameters between 0.3 mm and 0.6 mm, resulting in a 40% stiffness difference compared to natural bone, affirming its suitability for biomimetic applications. This innovative approach achieves an 86% weight reduction compared to titanium-based implants, significantly enhancing comfort, reducing physical strain, and improving mobility for amputees. By leveraging advanced topology optimisation and material science, this research provides valuable insights into lightweight and high-performance orthopaedic implant development.

Keywords: Lattice structures; Gait Cycle; Biomedical Implants; Finite Element Approach; Orthopedic Applications.

*Corresponding Author: Mr Karthikeyan Ramachandran

Email: K1825123@kingston.ac.uk & karthikeyan506@gmail.com

Introduction

The successful long-term implantation of orthopaedic devices relies on a crucial aspect of ensuring compatibility between the mechanical and structural characteristics of the implant and the human body [1]. However, a noteworthy challenge, aseptic late failure poses a significant threat with stress shielding (or stress protection) emerging as a primary biomechanical contributor to this hurdle. This phenomenon happens when the implant's stiffness substantially surpasses that of the surrounding bone, resulting in periprosthetic bone resorption due to decreased loading on the adjacent bone [2, 3]. This underscores the imperative for achieving precise biomechanical conformity to ensure the enduring resilience of orthopaedic interventions.

To address similar phenomena, cellular or lattice structures have attracted considerable attention due to their unique characteristics, including an extremely lightweight nature, high specific strength, and robust energy absorption capabilities [4, 5, 6, 7]. These qualities make lattice structures highly promising for applications in diverse fields such as acoustics, aerospace, and machinery industries [8, 9, 10]. Furthermore, the outstanding design flexibility of lattice structures in optimizing parameters like strut size, pore morphology, and macroscopic apparent density holds the potential to accelerate bone tissue regeneration or simulate stress stimuli in specific regions of primary bones [11]. These versatile features make them particularly valuable in the fields of orthopaedics and bioengineering [12]. For instance, Van Bael *et al.* investigated the impact of factors such as pore size, shape, porosity, and permeability on the mechanical responses and in vitro biological performances of scaffolds. Their study demonstrated that specific morphological modifications were deemed beneficial in enhancing cell seeding [13].

The strength of fixation for biological attachment relies significantly on the initial stability of the fixation, as excessive relative motion between bone and prosthesis can impede the osseointegration process [14]. In-vivo observations in a study conducted by Jasty *et.al.* disclosed bone ingrowth at the bone–prosthesis interface with micromotion ranging from 20 to 50 μm [15]. However, when the micromotion exceeded 50–150 μm, formation of fibrocartilage or fibrous tissues occurred instead, compromising the fixation strength, and potentially leading to component loosening [15, 16]. Various factors can generate loading on an implant, leading to micromotion characterized by the displacement of the implant in relation to the surrounding bone. These factors include the physical attributes of bone tissues, such as elastic moduli and

the strength of attachment between the implant and tissue, the mechanical interplay between the implant and tissue, and the geometric features of the implants [17]. To evaluate micromotion, these factors have been simulated using finite element (FE) investigations. The analysis explores component characteristics, including the stem and fixation pegs/screws, along with material and geometry considerations that could impact the interfacial conditions for osseointegration. [18, 19]. For instance, Wazen *et al.* demonstrated that in stable implants, bone formation consistently occurred around the implants. However, in implants subjected to micromotion, bone regeneration was disrupted in areas with high strain concentrations, while lower strain values facilitated bone formation [17]. Numerous efforts have been undertaken to mitigate bone resorption and enhance the stability of the bone-implant interface during micromotion. These endeavours involve integrating multiscale mechanics and topology optimization techniques to design porous architected biomaterials [20, 21]. In this context, engineering scaffolds play a crucial role, addressing segmental bone defects within a surrounding bone tissue environment characterized by diverse structures and biomechanical performances [22]. Various studies have explored the influence of materials, pore size, pore diameter, and permeability, and a direct correlation with bone growth has been indicated, displaying some asymptotic trends [11, 23, 24, 25].

However, the correlation between pore size and diameter with micromechanics has not been well-established, necessitating additional analysis. This research aims to bring a heightened understanding to the intricacies of micromotion during the gait cycle, focusing on lattice structures composed of three distinct evolving materials, with variations in pore sizes and diameters.

Design & Methodology

Material Selection

The material selection towards research was grounded in the utilization of three major alloys commonly employed in biomedical and orthopaedic applications. Careful considerations were given to essential factors including biocompatibility, mechanical strength, and manufacturing ease. According to literature, selected alloys include TNTZ alloy, with a composition as reported in [26], AZ91D magnesium alloy with a composition detailed in [27] and a Nickel Titanium-based shape memory alloy with a composition obtained from [28]. These alloys were chosen based on specific criteria encompassing biocompatibility, mechanical strength, and ease of manufacturing. The mechanical properties of these alloys are detailed in Table 1.

Table 1. Mechanical properties of selected alloys for the orthopedic applications.

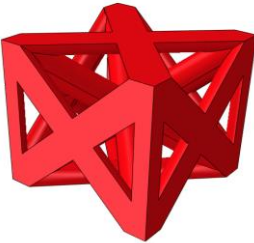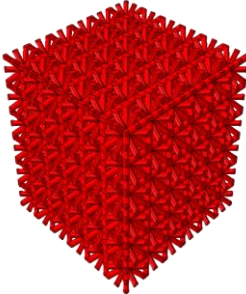| Alloys	Young's Modulus (GPa)	Density (g/cm³)	Poisson's Ratio	Average Tensile Strength (MPa)	Average Compressive Strength (MPa)
TNTZ Alloy	80	5.7	0.375	650	750
AZ91D	45	1.8	0.35	347	390
Ni-Ti SMA	40.1	6.45	0.3	745	790

Design of Unit Cell & Lattices
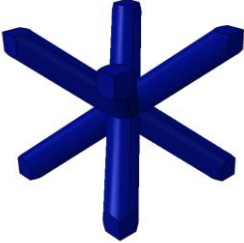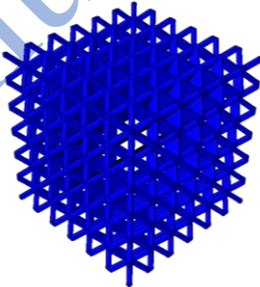
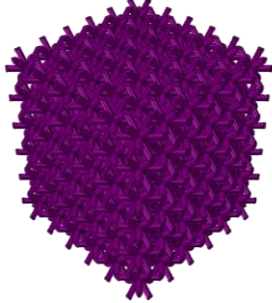| Unit cell-Type	Unit Cell – Structure	Strut Diameter (mm)	Strut Dimensions (l × b × h) (mm)	Lattice	Lattice Dimension (l × b × h) (mm)
BCC		0.8	5 × 5 × 5		30 × 30 × 30
FCC		0.8	5 × 5 × 5		30 × 30 × 30
FBCC		0.8	5 × 5 × 5		30 × 30 × 30

Figure 1. Designed unit cell and its associated lattice structure with its dimensions.

Three different unit cells i.e., face centred cubic (FCC), body centred cubic (BCC), and face-body centred cubic (FBCC) were designed and developed via SolidWorks 2019. The design as based on two key factors i.e., strut thickness (t) and unit cell size (a) which govern the overall geometry allowing the cell to be modified based on scale, porosity and pore size resulting in lattice structures. The unit cells were designed with same edge length, circular cross-section, and strut diameter. The developed units were generated into uniform lattices to evaluate the mechanical characteristics based on design and materials using Creo Parametric 9.0. The dimensions of unit cell and lattices are reported in Fig. 1.
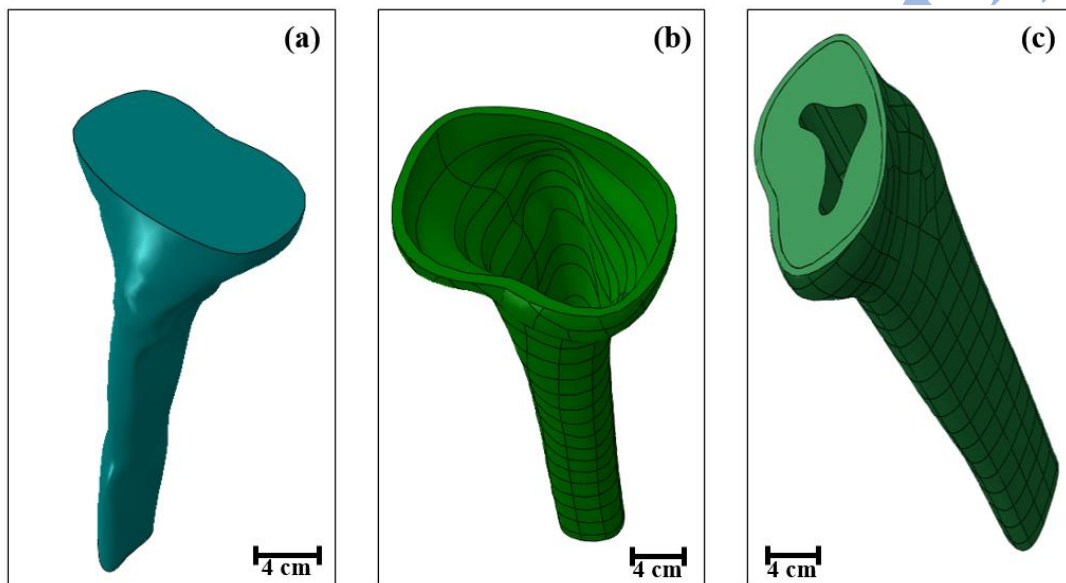
Design of Bones & Orthopaedic Implants

Figure 2. Designed tibia bone components (a) trabecular bone, (b) cortical bone and (c) final tibia bone for FEA with implant section.

The model towards this study was designed as showcased in Fig. 2 and to facilitate Finite Element Approach (FEA), the design was sectioned at 19 cm from the top surface to result a flat end. The design was divided into cortical and trabecular components through Boolean operations as reported in Fig. 2(a) & Fig. 2(b) for precise FEA analysis by considering varying material properties within bone. The tibia implant was also designed based on the cross-sectional dimension of bone with a press-fit configuration comprising two components i.e., top plate and a short stem as reported in Fig. 3. While the short stem is conventionally designed as a solid structure, this study tends to replace the solid stem with lattice structures.
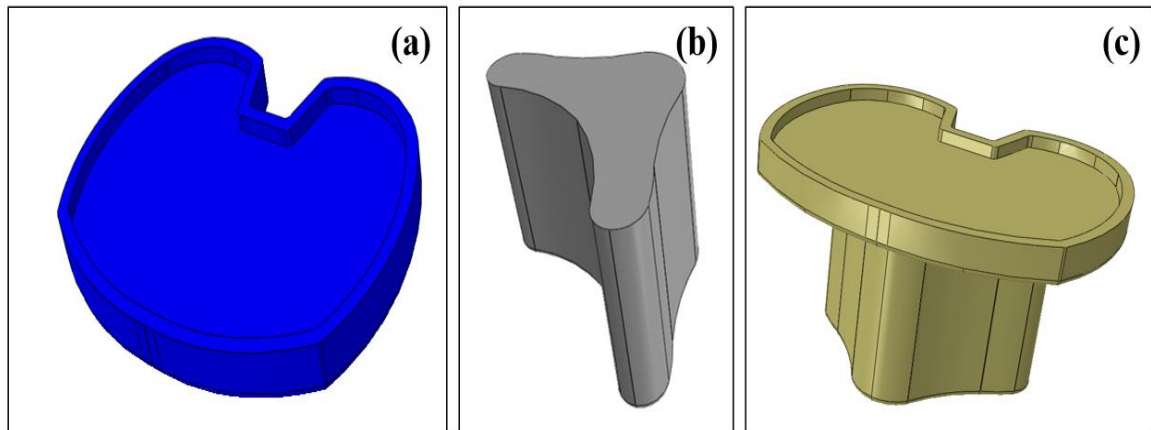
Figure 3. Design of tibia implant (a) top plate, (b) stem and (c) implant assembly
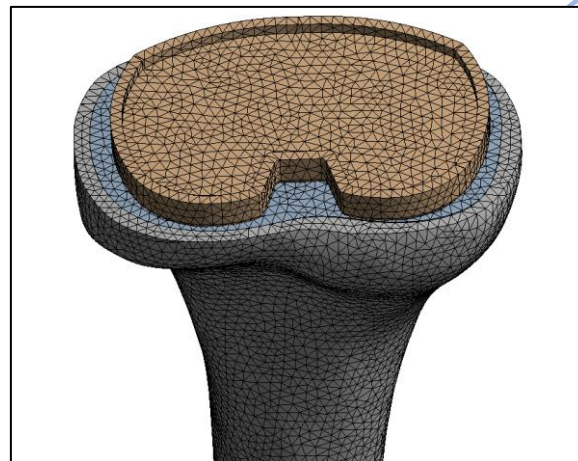
Finite Element Approach

Figure 4. Assembled structure of tibia implant with bone.

The effect of lattices on the implant and its micromechanics was analysed using the finite element method (FEM) in Ansys through static structural and dynamic simulations. Lattices developed from FCC, BCC, and FBCC unit cells were investigated to evaluate the suitability of the chosen alloys under mechanical loading. To assess the materials, the lattices were subjected to a virtual compression test in Ansys. Boundary conditions were imposed to replicate real-world constraints: the lower part of each lattice was firmly supported, while a deformation rate of 1 mm/s was applied to the top layer in the downward vertical direction. The loading duration was set at 60 seconds, during which the equivalent stress and total deformation were calculated. Figure 4 illustrates the assembled implant used in the FEM analysis. To ensure optimal geometric compatibility, the lattice structures were embedded into the tibia bone model through a meticulous design and analysis process. The tibia bone model was divided into cortical and trabecular components to facilitate precise FEA, allowing for an accurate representation of the bone's varying material properties. The tibia implant was

designed with a press-fit configuration which is consider to a common configuration and comprising two main components: a top plate and a short stem. The short stem, which is conventionally solid, was replaced by lattice structures in this study. Three different lattice structures were designed using SolidWorks and Creo Parametric, with specific dimensions for unit cells and struts to ensure they fit within the geometric constraints of the tibia bone.

Gait Loading Cycles in Tibia Implant

Table 2. Gait loading case cycles in Tibia Implant

Loading Case	Force (N)			Moments (N$_{mm}$)		
	Fx	*Fy*	*Fz*	*Mx*	*My*	*Mz*
Level Knee Bending	75.8	8.3	-2537.5	13220	12030	-2230
20% of gait cycle (Level Walking)	-76.05	169.96	-318.9	2420	3430	-1900
30% of gait cycle (Level Walking)	-144.65	-52.79	-1442.14	3760	-4790	1090

To analyse stress shielding and micromotion, gait loading cycles and deep knee bending cycles were simulated, representing common physiological conditions encountered by a knee implant. Three different loading scenarios, with load distributions shown in Table 2, were employed to mimic typical physiological stresses experienced by the human body. These loading conditions were derived from in-vivo measurements from an instrumented knee joint designed for a male subject weighing 1000 N, with a contact load error rate of less than ~2% [29, 30]. The tibial implant was modelled as a press-fit configuration to prevent rigid body motion, with the distal end of the tibia bone fixed. The implant's top plate was in contact with both the trabecular and cortical bone, with a friction coefficient of 0.35 applied to the interface between these surfaces. To restrict non-linear deformations, the displacement support tool in Ansys was employed, limiting movement to the z-axis. A coordinate system was established through the centre of the implant's top surface, and forces (Fx, Fy, Fz) and moments (Mx, My, Mz) were applied along the respective x, y, and z axes. Positive values were assigned to forces and anticlockwise moments along these axes. Loads and moments were applied on the top surface of the implant's plate to simulate realistic boundary conditions. Mesh convergence analysis was performed with element sizes ranging from 0.1 mm to 1 mm to ensure accurate and reliable results.

Results & Discussion
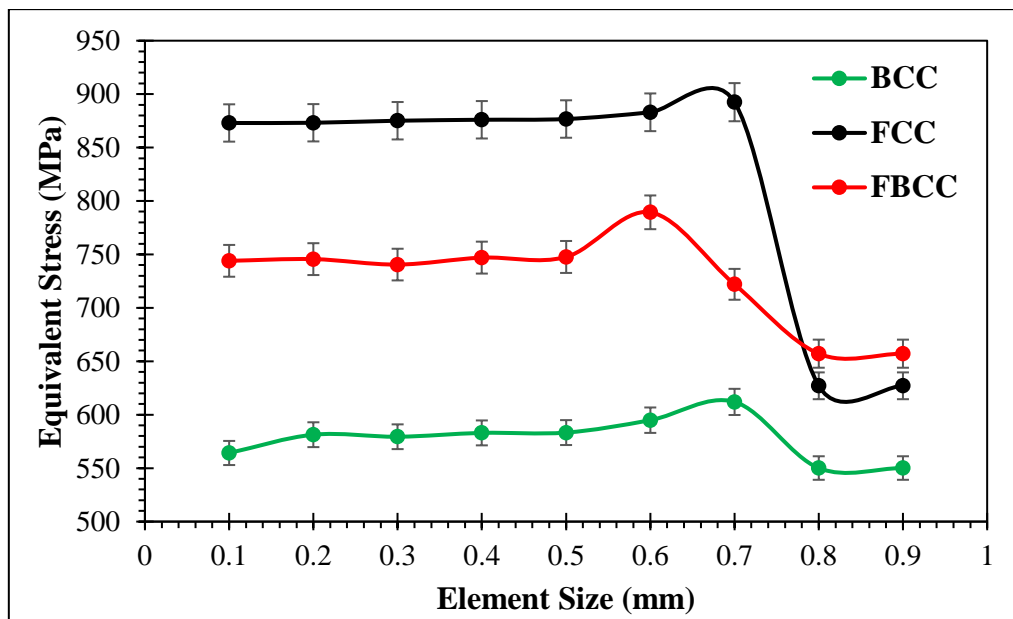
Compressive test - lattices

Figure 5. Mesh convergence study for lattices with respect to varying element size for TNTZ alloy.

Compression test was carried out on each lattice structures via FE approach with help of the chosen materials properties. Three distinct materials each employing BCC, FCC and FBCC lattice structures were subjected to testing to determine the material for micro-mechanics simulations. Mesh convergence studies were conducted for all scenarios, revealing a spectrum of mesh convergence rather than a uniform converging mesh size. Figure 5 illustrates the convergence study conducted towards the lattices for TNTZ alloy. The study was conducted via direct optimisation where the mesh element size was set as the input parameter for the convergence study, with Equivalent Stress (Von-Mises) assigned as the output parameter. The element size of mesh was varied between 0.1 to 1 mm and the convergence of equivalent stress was identified at 0.5 mm. Figure 5 illustrates the relationship between element size and equivalent stress for BCC, FCC and FBCC structures. For FCC and FBCC, equivalent stress stabilizes between element sizes of 0.1 mm and 0.6 mm, indicating convergence, while a significant drop occurs beyond 0.7 mm. In contrast, BCC shows fluctuating stress values across all element sizes, suggesting a lack of convergence making 0.5 mm as optimal element size as it offers a balance between computational efficiency and result accuracy. The lack of convergence in BCC results is likely due to its inherent material behaviour and sensitivity to stress gradients. The BCC lattice structure due to its intricate and complex behaviour results in

complex element and node development resulting in drop of mesh elements quality which affects the aspect ratios and minimal distortion leading to convergence issues.

Table 3 reports the equivalent stress attained from FE analysis for all three lattices under distinct material properties. From the Table 3, it could be noted that FCC showcased higher equivalent stress distribution compared to BCC and FBCC structures in all three alloys. However, while analysing the stress distribution plot reported in Fig. 6, it could be stated that maximum distribution occurs on the top surfaces and strut connections in the lattices [31, 32]. From Fig. 6, it could be stated that stress distribution was more uniform in FCC and FBCC compared to BCC. The non-uniform distribution of the stress in BCC is aligned with previous research [32, 33]. This non-uniform distribution could have been attributed to the struct design of BCC which transfers load to the cores and edges of the lattice rather than to the internal struts.

Table 3. Equivalent stress for various lattices attained via FE analysis for various alloys

Lattices	Equivalent Stress (MPa)		
	TNTZ Alloy	**AZ91D Alloy**	**Ni-Ti SMA**
BCC	550.11	400.69	380.38
FBCC	657.12	479.18	438.34
FCC	627.06	676.78	621.36

Figure 6 illustrates the equivalent stress distribution of lattices with TNTZ alloy as material. From Fig. 6, it could be stated that stress distribution was more uniform in FCC and FBCC compared to BCC. The non-uniform distribution of the stress in BCC is aligned with previous research [32, 33]. This non-uniform distribution could have been attributed to the struct design of BCC which transfers load to the cores and edges of the lattice rather than to the internal struts. The stress cases also (Fig. 6) demonstrates that TNTZ alloy possessed greater stiffness which resulted in elevated stress in operational conditions whereas Ni-Ti SMA tends to induce the least equivalent stress. It is crucial to emphasise that from a mechanical standpoint selecting a material with higher stiffness is essential for load bearing. However, when considering biocompatibility, the material should ideally have a stiffness like that of natural human bone to prevent undesirable conditions like stress-shielding and micromotion. AZ91D alloy showcased a good equivalent stress distribution with minimal high stress points with good biocompatibility equal or more than to that of TNTZ and Ni-Ti SMA making it a preferred choice for micromechanics study. Furthermore, density of AZ91D makes it one of the best choices towards tibia implants as its closer to that of human bones [34, 35].
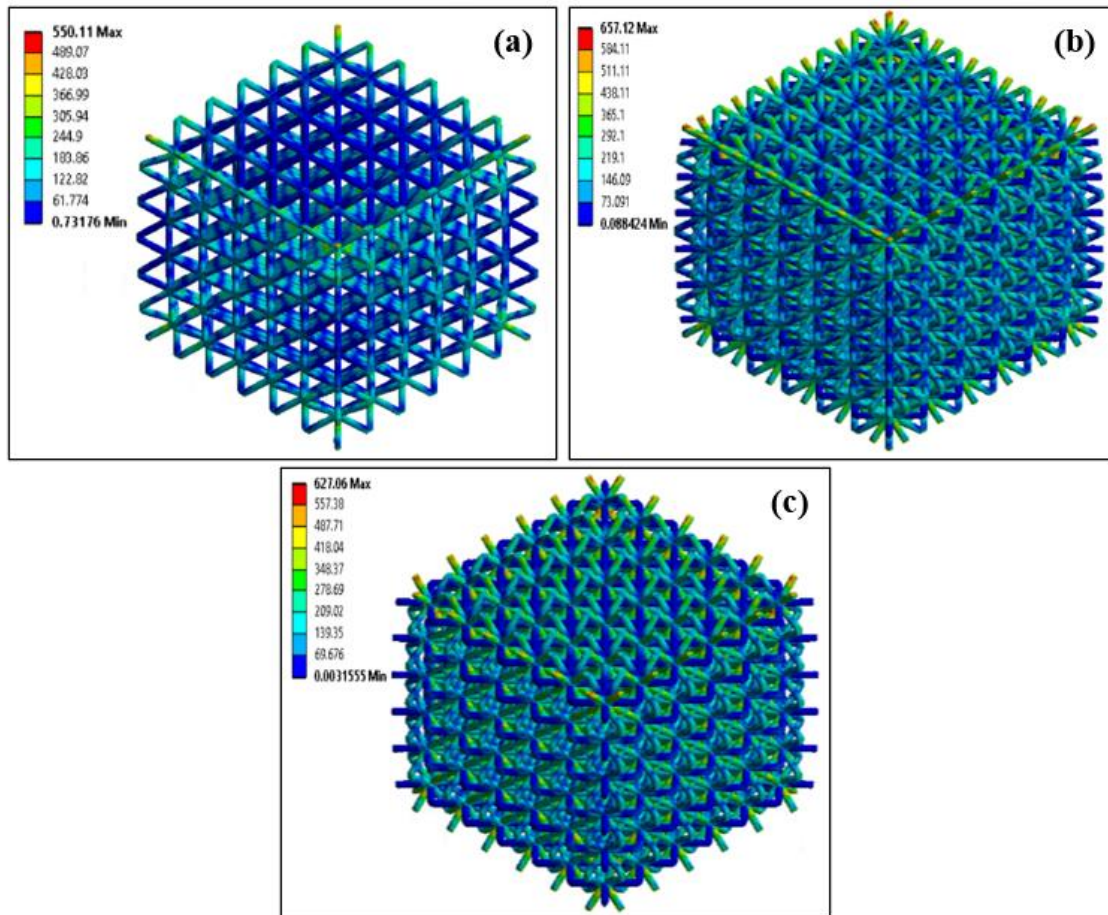
Figure 6. Equivalent stress distribution of lattices (a) BCC, (b) FBCC and (c) FCC with TNTZ alloy as material properties

Gait Loading Behaviour

Table 4. FEA results of Equivalent stress distribution towards three different lattices with AZ91D as material

Gait Cycle	Equivalent Stress (MPa)		
	BCC	FBCC	FCC
Level Bending	36.824	31.08	38.409
20% of gait cycle (Level walking)	4.8086	3.9996	5.9162
30% of gait cycle (Level Walking)	17.564	18.992	39.093

Based on compressive studies, AZ91D was utilised as the material towards gait loading cycles studies through FEA approach. The mesh was similar to that of previous compressive study as determined through optimisation. The boundary conditions were based on the Table 2 with bottom of the bone was set as a fixed. Table 4 reports the equivalent stress attained via FEA towards three lattices with AZ91D as the material under various gait loading conditions. The FEA results showcased a distinct change in the equivalent stress towards the lattices. From Table 4 in terms of level bending, FCC displayed the highest equivalent stress distribution

which was ~6% and ~19% more than BCC and FBCC. The lattice structures were embedded into the tibia bone model as described in methodology, and their mechanical behaviour was analysed using FEA in Ansys. Boundary conditions were applied to replicate real-world constraints, such as firmly supporting the lower part of each lattice and applying a deformation rate to the top layer. Furthermore, lattice structures were embedded into tibia through a bonded approach with small amount of frictional coefficient allowing to understand the contact stress distribution between structure and tibia implant. Also, lattice structures were designed to match the cross-sectional dimensions of the tibia bone, ensuring a snug fit within the bone's geometry. The press-fit configuration helped in achieving optimal geometric compatibility, as it prevented rigid body motion and ensured the implant remained securely in place.

Figure 7 illustrates the equivalent stress distribution during level bending for the BCC lattice structure. It shows that most struts in the BCC lattice are subjected to almost the same stress value, with a few struts at the outer periphery carrying minimal stress. The extreme stress points are located at the base of implant where it touches the body, indicating areas of high load transfer. The uniform stress distribution within the lattice structure suggests that the design is well-integrated into the tibia bone, ensuring optimal load transfer and minimizing stress concentrations. By carefully designing the lattice structures to fit within the tibia bone's geometry and using a press-fit configuration, the study ensures that the implants achieve optimal geometric compatibility. This approach not only enhances the mechanical performance of the implants but also promotes better integration with the surrounding bone tissue, reducing the risk of stress shielding and improving overall implant stability.
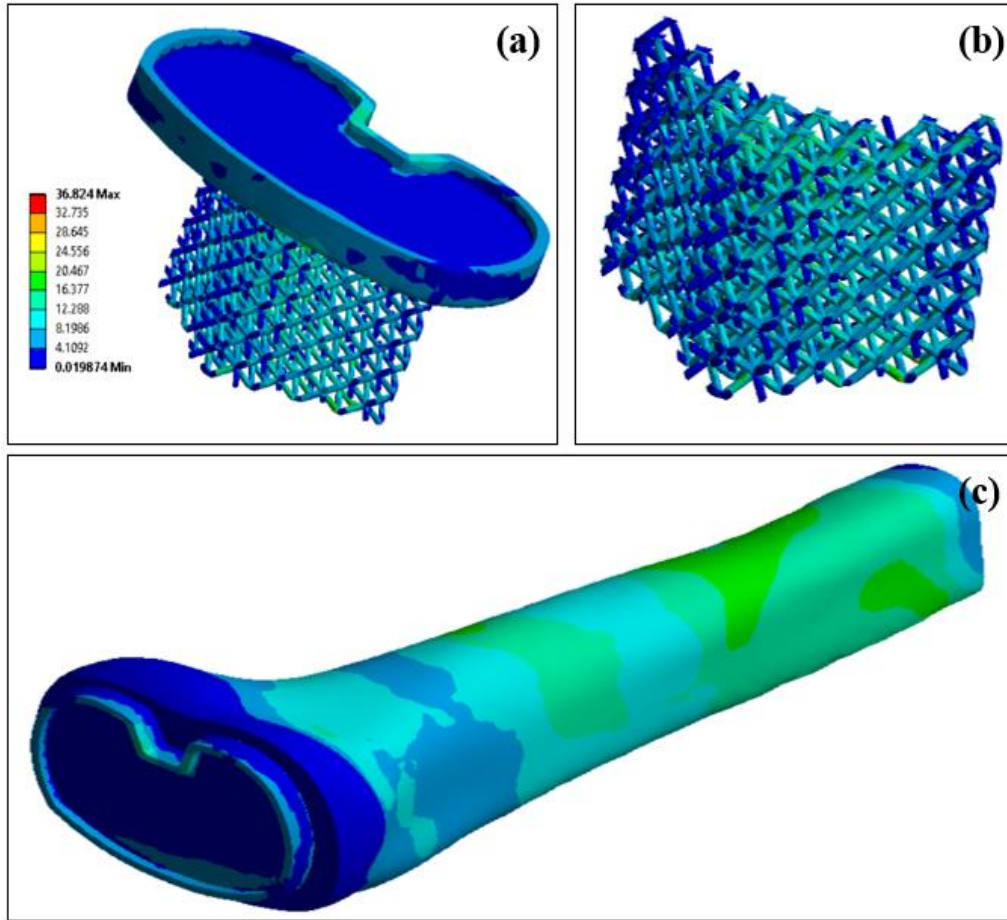
Figure 7. Equivalent stress distribution during level bending for BCC (a) With tibia bone implant, (b) BCC lattice and (c) complete bone structure

On the other hand, FCC indicated three distribution regions (Fig. A1) with inner region filled with higher stress, followed by a reduced stress distribution in other areas and half of the outer region is subjected to the minimum stress. FBCC lattice demonstrated superior performance with the lowest equivalent stress. This underscores the importance of lattice geometry in influencing stress distribution during bending loads, where the FBCC lattices structural configuration proves advantageous in minimizing stress concentrations. The stress distribution of FBCC shows variations in the face and central struts. In level bending, most of the outer surfaces are subjected to minimal stress distribution, while the internal strut elements carry more than average stress. Among these, in most regions, the central struts develop nearly the maximum stress reported in the whole structure. In BCC, as the load increased to 20% (Fig. A 2) and 30% of level walking, stress distribution shifted towards inner portion of the stem with more outer struts experiencing minimal stress. Notably, at 30% load, stress distribution became more evenly distributed throughout the stem, resembling that of level bending conditions. The lattice Intersection points of unit cells consistently exhibited an average stress level across all

loading conditions. Likewise in FCC at 20% (Fig. A2) of level walking, stress concentration in the higher stress regions decreased, while the minimum stress region expanded on the outer surface. By 30% of level walking, outer surface predominantly consisted of less stressed regions, replacing areas with average stress concentration. Intersection points displayed a combination of extreme minimum and below-average stress values. In all the cases, the stress distribution in BCC and FCC shows non-uniformity stress distribution throughout the structure. This observed behaviour could have been attributed to the lattices structure to evenly distribute loads and minimise stress concentrations [36, 37].
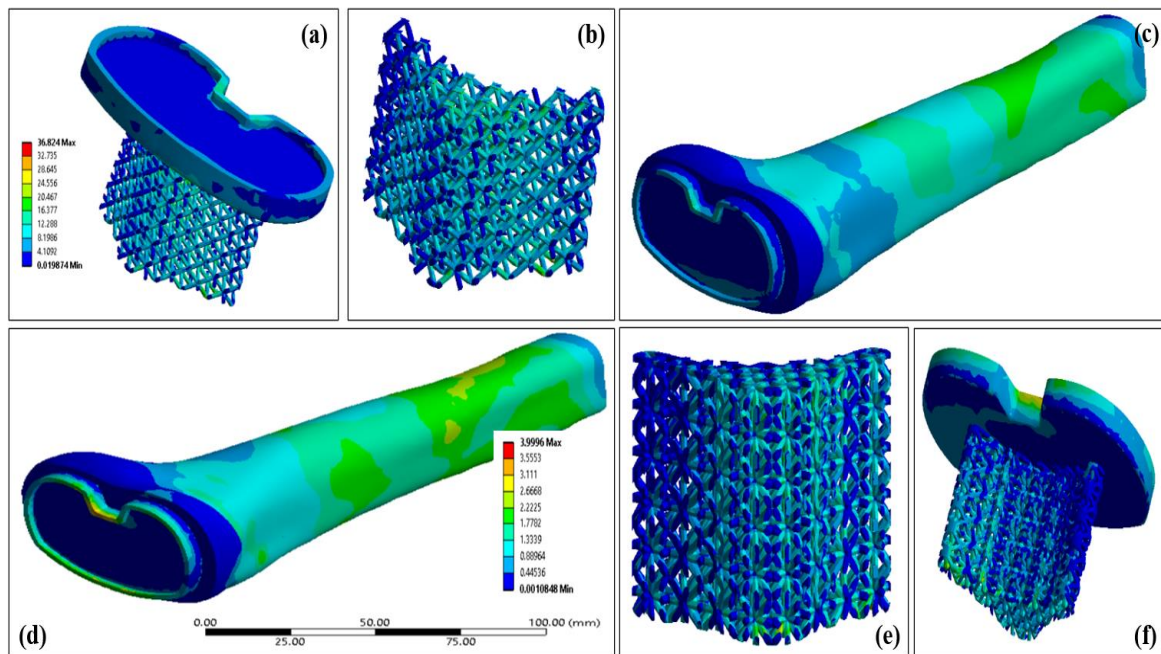

Figure 8. Equivalent stress distribution of FBCC (a, b, & c) at 20% level bending and (d, e, & f) at 30% level bending

On contrary, equivalent stress distribution of FBCC lattice structure is illustrated in Fig. 8 where stress distribution varied between the face and central struts. At 20% of the gait cycle, minimum stress region on the outer surface expanded non-uniformly. Upon further loading to 30%, this minimum stress region exhibited uniformity across the structure. Junction/intersection points demonstrated a uniform circular stress distribution pattern, with minimum stress reported throughout the lattices. This uniformity in stress distribution was different compared to FCC and BCC lattices which might have been attributed towards the combined properties of FBCC which is a hybrid build of FCC and BCC. Furthermore, FBCC structure develops less stress as compared to BCC and FCC and the stress patterns are more reliable due to the arrangement of struts. The strut arrangement supported the load transfer more smoothly resulting in better mechanical. Further, the arrangement of struts could have

also enhanced the biological compatibility owing to its pore's distribution [38]. On the other hand, in FCC and BCC stem the strut design becomes less efficient in channelling the load through it causing higher stress distribution [39, 40].

Table 5. Maximum total deformation of the lattices with respect to gait cycle

Gait Cycle	Total Deformation (mm)		
	BCC	FBCC	FCC
Level Bending	2.9865E-3	6.5566E-4	1.1394E-3
20% of gait cycle (Level walking)	6.6954E-4	2.5671E-4	3.993E-4
30% of gait cycle (Level Walking)	1.2249E-2	9.1406E-3	8.5934E-3

The gait cycles introduce micromotion i.e., total deformation on the of the implant with different magnitudes as tabulated in Table 5 and Fig. A3. In BCC structure, most struts undergo their highest deformation across the entire structure during normal bending load conditions, with the least deformation observed in the upper edge struts during 20% level walking, gradually decreasing towards the lower struts. Moreover, 30% increase in walking level leads to a further reduction in the region of maximum deformation, notably affecting the base area. Meanwhile, FBCC structure shows consistent deformation under level bending, with maximum deformation concentrated within a confined area, gradually diminishing from top to bottom. During 20% of level bending, most struts experience maximum stress distribution which diminishes further with a 30% increase in the gait cycle.

Similarly, in FCC structure, level bending induces consistent deformation with maximum deformation localized at top and decreasing towards the base unit cell. During 20% of level walking, maximum deformation is concentrated on one extreme side of the unit cells, decreasing gradually towards the opposite side, and further diminishing with a 30% increase in level walking. Among these, FBCC indicated the minimum micromotion in most of the load cases. The stress developed with FBCC structure is the least among the others due to the arrangement of struts in the lattice structure, which makes the body more rigid to withstand micromotion. By analysing the total deformation of lattices, it could be stated that all the three lattices were in closer proximity towards the micro-mechanics requirements [41]. Further, the combination of FCC and BCC attributes in the FBCC provides a combined enhanced mechanical property as well as strut behaviour which increases the load transfer capabilities of FBCC. Furthermore, FBCC might have higher packing efficiency due to its combination of

FCC and BCC owing to closely packed intersectional joints leading to more ductile behaviour [42].

The comparison between lattice structures (FCC, BCC, FBCC) and conventional solid implants reveals notable differences in stress distribution, micromotion, and load transfer. While current solid materials provide strong mechanical properties and corrosion resistance, they exhibit a pronounced stiffness mismatch with natural bone, contributing to stress shielding effects [43, 17]. Moreover, traditional implants are associated with a higher risk of micromotion at the bone-implant interface, potentially leading to implant loosening [44]. In contrast, FBCC lattices demonstrated superior performance, offering more uniform stress distribution and lower equivalent stress compared to FCC and BCC, thereby reducing the risk of stress shielding commonly seen in solid implants [45]. FBCC lattices also exhibited minimal micromotion, particularly under gait cycle loading, promoting implant stability and enhancing bone ingrowth [43]. Conversely, BCC and FCC lattices showed higher deformation and less efficient load transfer, similar to conventional implants. The optimized porosity and strut arrangement in FBCC improve biological compatibility by facilitating bone growth and reducing localized stress concentrations [45]. These findings suggest that FBCC lattice structures may offer improved long-term outcomes over traditional implants by optimizing mechanical performance and biological integration.

Effect of strut diameter

Table 6. Strut diameter and its effect at 20% Gait cycle for FBCC

Strut Diameter (mm)	Maximum Total Deformation (mm)	Equivalent stress (MPa)
0.6	5.5209E-4	6.8444
0.5	5.8353E-4	5.9872
0.4	6.2304E-4	5.064
0.3	6.8354E-4	4.6482

The superior performance of FBCC lattices in stress distribution, micromotion, and load transfer is closely linked to the optimization of strut diameter, which plays a critical role in determining the mechanical behaviour of lattice structures. To understand the effect of lattice structure on mechanical performance with respect to strut diameter, a 20% bending load was applied via a direct optimization approach using FEA on FBCC lattice structures. Table 6 reports the effect of varying strut diameters on deformation and equivalent stress. Four distinct strut diameters—0.3 mm, 0.4 mm, 0.5 mm, and 0.6 mm were analysed, which would reduce

overall porosity by approximately 50%, as strut diameter and porosity are inversely correlated [46].

The relationship between strut diameter and stiffness can be attributed to the mechanics of lattice structures. Larger strut diameters increase the cross-sectional area of the struts, which enhances their ability to resist deformation under load. This results in a higher Young's modulus and greater overall stiffness of the lattice structure [47]. However, this increased stiffness can lead to a higher concentration of stress within the implant, potentially causing stress shielding. Stress shielding occurs when the implant is significantly stiffer than the surrounding bone, leading to reduced mechanical stimulation of the bone and subsequent bone resorption [48]. Conversely, smaller strut diameters reduce the cross-sectional area of the struts, making the lattice structure more flexible and less stiff. This flexibility allows for better load distribution and reduces the risk of stress shielding, as the implant's mechanical properties are more closely matched to those of natural bone [49]. However, the reduced stiffness can also compromise the mechanical integrity of the implant under higher loads, potentially leading to deformation or failure.

From the data in Table 6, it can be concluded that as the strut diameter decreases, the lattice structure loses stiffness, leading to less efficient load distribution. For example, a lattice with a 0.3 mm strut diameter exhibited a calculated Young's modulus of ~30 GPa, which is ~40% closer to the modulus of natural bone (~ 7-30 GPa, depending on the bone type and location) [50]. This similarity in modulus is desirable as it minimises the risk of stress shielding, where a significant mismatch in stiffness between the implant and bone can result in bone resorption [51]. However, as the strut diameter increases to 0.6 mm, the Young's modulus increases by ~44%, indicating greater stiffness, but at the expense of higher implant rigidity, which could lead to stress shielding [52]. The inverse relationship between stiffness and deformation is also evident: as stiffness decreases with smaller strut diameters, total deformation increases. The FEA results show that the lattice with the smallest strut diameter (0.3 mm) experienced the highest deformation, compromising the implant's ability to effectively transfer load. In contrast, a strut diameter of 0.5 mm was found to be optimal, balancing stiffness and porosity to minimize deformation while avoiding excessive rigidity. Increasing porosity further enhanced deformation, suggesting that overly porous structures may compromise mechanical integrity, particularly under higher loads. Various literatures support this finding, indicating that lattice structures with lower porosity exhibit higher stiffness and reduced deformation, but also emphasize the need for balance [53]. Overly stiff implants can lead to stress shielding,

while highly porous structures may lose mechanical strength and durability. In conclusion, the optimized strut diameter of 0.5 mm offers a compromise between mechanical stiffness and porosity, ensuring efficient load transfer while reducing the risk of implant failure due to excessive deformation or stress shielding. Thus, optimization of strut diameter is critical for designing lattice structures that provide the necessary mechanical support while minimizing the risk of stress shielding. A strut diameter of 0.5 mm offers a compromise between mechanical stiffness and porosity, ensuring efficient load transfer and enhancing the implant's performance and longevity. This diameter closely mimics the mechanical properties of natural bone, making it ideal for orthopaedic applications.

Conclusion

This research accesses the design and development of orthopaedic implants using three distinct lattice structures: Face Centred Cubic (FCC), Body Centred Cubic (BCC), and a hybrid structure Face-Body Centred Cubic (FBCC) with help of Finite Element Analysis (FEA). Three materials Ni-Ti Shape Memory Alloy (SMA), TNTZ Alloy, and AZ91D alloy were selected towards the study and through compressive studies on lattices, AZ91D was identified as the optimal material for tibia bone implants. Gait cycle analyses, including loading level knee bending at 20% and 30% levels, revealed that FBCC exhibited superior performance across all three gait cycles due to its combined properties of BCC and FCC, resulting in higher load transfer behaviour. Furthermore, study explored the impact of porosity by varying the strut diameter (0.3 – 0.6 mm), demonstrating a marginal 40% difference in stiffness of FBCC compared to natural bone. This underscores the potential of the developed implant for future orthopaedic applications. This research significantly advances the field of orthopaedic implant materials and designs, showcasing the successful integration of biomimicry principles. The outcomes of this study hold promise for enhancing patient outcomes in orthopaedic applications, marking a notable contribution to the field.

Acknowledgement

Author Contribution

KR – Research idea creation and implementation, original & review draft writing, project management and supervision.

NN – Original draft writing, Simulation execution and Software

CLG – Original & Review draft writing

MNA – Research idea creation, simulation validation and original & review draft writing.

Data and Code Availability

The raw/processed data required to reproduce these findings cannot be shared at this time as the data also forms part of an ongoing study. There is no code availability towards this study.

Declaration of Competing Interest

Authors declare no completing interest towards this publication.

Ethical Approval

Not applicable.

References

[1] S. Bauer, P. Schumuki, K. Mark and J. Park, "Engineering biocompatible implant surfaces: Part I: Materials and surfaces," *Progress in Materials Science,* vol. 58, no. 3, pp. 261-326, 2013.

[2] S. Naghavi, C. Lin, C. Sun, M. Tamaddon, M. Basiouny, P. G-Souto, S. Taylor, J. Hua, D. Li, L. Wang and C. Liu, "Stress shielding and bone resorption of press-fit polyether–ether–ketone (PEEK) hip prosthesis: A sawbone model study," *Polymers,* vol. 14(21), no. 4600, 2022.

[3] M. B-Lipperman and A. Gefen, "A method of quantification of stress shielding in the proximal femur using hierarchical computational modeling," *Computer Methods in Biomechanics and Biomedical Engineering,* vol. 9, no. 1, pp. 35-44, 2006.

[4] H. Yin, F. Meng, L. Zhu' and G. Wen, "Optimization design of a novel hybrid hierarchical cellular structure for crashworthiness," *Composite Structures,* vol. 303, no. 116335, pp. 1-27, 2023.

[5] T. Maconachie, M. Leary, B. Lozanovski, X. Zhang, M. Qian, O. Faruque and M. Brandt, "SLM lattice structures: Properties, performance, applications and challenges," *Materials & Design,* vol. 183, no. 108137, pp. 1-18, 2019.

[6] L. Greco, F. Buccino, Z. Xu, L. Vergani, F. Berto, M. Gaugliano, N. Razavi and S. Bagherifard, "Design and Analysis of Energy Absorbent Bioinspired Lattice Structures," *Journal of Bionic Engineering,* vol. 20, pp. 1670-1686, 2023.

[7] S. Yeo, M. Oh and P. Yoo, "Structurally Controlled Cellular Architectures for High-Performance Ultra-Lightweight Materials," *Advanced Materials,* vol. 31, no. 34, 2018.

[8] Y. Ibrahim, Z. Li, C. Davies, C. Maharaj, J. Dear and P. Hooper, "Acoustic resonance testing of additive manufactured lattice structures," *Additive Manufacturing,* vol. 24, pp. 566-576, 2018.

[9] V. Vasiliev, V. Barynin and A. Razin, "Anisogrid composite lattice structures – Development and aerospace applications," *Composite Structures,* vol. 94, no. 3, pp. 1117-1127, 2012.

[10] G. Totaro and Z. Gurdal, "Optimal design of composite lattice shell structures for aerospace applicationsDesign ottimale di strutture a guscio lattice in composito per applicazioni aerospaziali," *Aerospace Science and Technology,* vol. 13, no. 4-5, pp. 157-164, 2009.

[11] D. Barba, E. Alabort and R. Reed, "Synthetic bone: Design by additive manufacturing," *Acta Biomaterialia,* vol. 97, pp. 637-656, 2019.

[12] M. Hedayati, M. Neufeld, M. Reynolds and M. Kipper, "The quest for blood-compatible materials: Recent advances and future technologies," *Material Science and Engineering: R: Reports,* vol. 138, pp. 118-152, 2019.

[13] S. Bael, Y. Chai, S. Truscello, M. Moesen, G. Kerckhofs, H. Oosterwyck, J. Kruth and J. Schrooten, "The effect of pore geometry on the in vitro biological behavior of human periosteum-derived cells seeded on selective laser-melted Ti6Al4V bone scaffolds," *Acta Biomaterialia,* vol. 8, no. 7, pp. 2824-2834, 2012.

[14] A. Mavrogenis, R. Dimitriou, J. Parvizi and G. Babis, "Biology of implant osseointegration," *J Musculoskelet Neuronal Interact ,* vol. 9, no. 2, pp. 61-71, 2009.

[15] M. Jasty, C. Bragdon, D. Bruke, D. O'Connor, J. Lowenstein and W. Harris, "In vivo skeletal responses to porous-surfaced implants subjected to small induced motions," *The Journal of Bone & Joint Surgery,* vol. 79, no. 5, pp. 707-714, 1997.

[16] H. Kienapfel, C. Sprey, A. Wilke and P. Griss, "Implant fixation by bone ingrowth," *The Journal of Arthroplasty,* vol. 14, no. 3, pp. 355-368, 1999.

[17] R. Wazen, J. Currey, H. Guo, J. Brunski, J. Helms and A. Nanci, "Micromotion-induced strain fields influence early stages of repair at bone–implant interfaces," *Acta Biomaterialia,* vol. 9, no. 5, pp. 6663-6674, 2013.

[18] M. Tissakht and A. Ahmed, "Tensile stress-strain characteristics of the human meniscal material," *Journal of Biomechanics,* vol. 28, no. 4, pp. 411-422, 1995.

[19] M. Keja, H. Wevers, D. Siu and H. Grootenboer, "Relative motion at the bone-prosthesis interface," *Clinical BIomechanics,* vol. 9, no. 5, pp. 275-283, 1994.

[20] A. Rahimizadeh, Z. Nourmohammadi, S. Arabnejad, M. Tanzer and D. Pasini, "Porous architected biomaterial for a tibial-knee implant with minimum bone resorption and bone-implant interface micromotion," *Journal of the Mechanical Behavior of Biomedical Materials,* vol. 78, pp. 465-479, 2018.

[21] S. Khanoki and D. Pasini, "Multiscale Design and Multiobjective Optimization of Orthopedic Hip Implants with Functionally Graded Cellular Material," *Journal of Biomedical Engineering,* vol. 134, no. 3, pp. 031004-031014, 2012.

[22] S. Jiang, M. Wang and J. He, "A review of biomimetic scaffolds for bone regeneration: Toward a cell-free strategy," *Bioengineering & Translational Medicine,* vol. 6, no. 2, 2021.

[23] M. Dias, P. Fernandes, J. Guedes and S. Hollister, "Permeability analysis of scaffolds for bone tissue engineering," *Journal of BIomechanics,* vol. 45, no. 6, pp. 938-944, 2012.

[24] J. Jiao, G. Hong, D. Zhang, M. Wang, H. Tang, J. Yang, X. Qu and B. Yue, "Influence of porosity on osteogenesis, bone growth and osteointegration in trabecular tantalum scaffolds fabricated by additive manufacturing," *Frontiers in BIoengineering and Biotechnology,* vol. 11, 2023.

[25] C. Song, L. Liu, Z. Deng, H. Lei, F. Yuan, Y. Yang, Y. Li and J. Yu, "Research progress on the design and performance of porous titanium alloy bone implants," *Journal of Materials Research and Technology,* vol. 23, pp. 2626-2641, 2023.

[26] A. Najdahmadi, A. Z-Hanzaki and E. Farghadani, "Mechanical properties enhancement in Ti–29Nb–13Ta–4.6Zr alloy via heat treatment with no detrimental effect on its biocompatibility," *Materials & Design,* vol. 54, pp. 786-791, 2014.

[27] G. Song, A. Atrens and M. Dargusch, "Influence of microstructure on the corrosion of diecast AZ91D," *Corrosion Science,* vol. 41, no. 2, pp. 249-273, 1998.

[28] S. Sadrnezhaad and S. Hosseini, "Fabrication of porous NiTi-shape memory alloy objects by partially hydrided titanium powder for biomedical applications," *Materials & Design,* vol. 30, no. 10, pp. 4483-4487, 2009.

[29] I. Kutzner, B. Heinlein, F. Graichen, A. Bender, A. Rohlmann, A. Halder, A. Beier and G. Bergmann, "Loading of the knee joint during activities of daily living measured in vivo in five subjects," *Journal of Biomechanics,* vol. 43, no. 11, pp. 2164-2173, 2010.

[30] B. Heinlein, I. Kutzner, F. Graichen, A. Bender, A. Rohlmann, A. Halder, A. Beier and G. Bergmann, "Complete data of total knee replacement loading for level walking and stair climbing measured in vivo with a follow-up of 6–10 months," *Clinical Biomechanics,* vol. 24, no. 4, pp. 315-326, 2009.

[31] B. Babamiri, B. Barnes, A. S-Teharani, N. Shamsaei and K. Hazeli, "Designing additively manufactured lattice structures based on deformation mechanisms," *Additive Manufacturing,* vol. 46, no. 102143, pp. 1-19, 2021.

[32] Z. Alomar and F. Concli, "Compressive behavior assessment of a newly developed circular cell-based lattice structure," *Materials & Design,* vol. 205, no. 109716, pp. 1-9, 2021.

[33] N. Jin, F. Wang, Y. Wang, B. Zhang, H. Cheng and H. Zhang, "Failure and energy absorption characteristics of four lattice structures under dynamic loading," *Materials & Design,* vol. 169, no. 107655, pp. 1-11, 2019.

[34] J. Yang, R. Chiou, A. Ruprecht, J. Vicario, L. MacPhail and T. Rams, "A new device for measuring density of jaw bones," *Dentomaxillofacial Radiology,* vol. 31, no. 5, pp. 313-316, 2002.

[35] H. E. Meema and S. Meema, "Compact Bone Mineral Density of the Normal Human Radius," *Acta Radiologica: Oncology, Radiation, Physics, Biology,* vol. 17, no. 4, pp. 342-352, 1978.

[36] H. Fan, F. Jin and D. Fang, "Characterization of edge effects of composite lattice structures," *Composites Science and Technology,* vol. 69, no. 11-12, pp. 1896-1903, 2009.

[37] M. Benedetti, A. d. Plessis, R. Ritchie, M. Dallago, N. Razavi and E. Berto, "Architected cellular materials: A review on their mechanical properties towards fatigue-tolerant design and fabrication," *Materials Science and Engineering: R: Reports,* vol. 144, no. 100606, 2021.

[38] N. Abbasi, S. Hamlet, R. Love and N. Nguyen, "Porous scaffolds for bone regeneration," *Journal of Science: Advanced Materials and Devices,* vol. 5, no. 1, pp. 1-9, 2020.

[39] A. d. Plessis, N. Razavi, M. Benedetti, S. Murchio, M. Leary, M. Watson, D. Bhate and F. Berto, "Properties and applications of additively manufactured metallic cellular materials: A review," *Progress in Materials Science,* vol. 125, no. 100918, pp. 1-43, 2022.

[40] L. Bai, C. Yi, X. Chen, Y. Sun and J. Zhang, "Effective Design of the Graded Strut of BCC Lattice Structure for Improving Mechanical Properties," *Materials,* vol. 12, no. 13-2192, pp. 1-24, 2019.

[41] S. Small, R. Rogge, R. Malinzak, E. Reyes, P. Cook, K. Farley and M. Ritter, "Micromotion at the tibial plateau in primary and revision total knee arthroplasty: fixed versus rotating platform designs," *Bone & Joint Research,* vol. 2016, no. 5(4), pp. 122-129, 2016.

[42] O. Soloveva, S. Soloveva, A. Talipova, R. Shakurova and D. Paluku, "Study of heat transfer in models of FCC, BCC, SC and DEM porous structures with different porosities," in *Journal of Physics: Conference Series, Volume 2373, Applied Physics, Materials Analysis and Characterization,* 2022.

[43] R. Burchard, J. Graw, C. Soost and J. Schmitt, "Stress shielding effect after total hip arthroplasty varies between combinations of stem design and stiffness—a comparing biomechanical finite element analysis," *International Orthopaedics,* vol. 47, pp. 1981-1987, 2023.

[44] X. Gao, M. Fraulob and G. HaIat, "Biomechanical behaviours of the bone–implant interface: a review," *Journal of the royal society interface,* vol. 16, no. 156, pp. 1-20, 2019.

[45] L. Gibson and M. Ashby, Cellular Solids: Structure and Properties, Cambridge: Cambridge University Press, 1997.

[46] C. Qiu, S. Yue, N. Adkins, M. Ward, H. Hassanin, P. Lee, P. Withers and M. Attalah, "Influence of processing conditions on strut structure and compressive properties of cellular lattice structures fabricated by selective laser melting," *Materials Science and Engineering: A,* vol. 628, pp. 188-197, 2015.

[47] P. Hanzl, I. Zetkova and S. Cajthamlova, "Influence of Strut Diameter and Building Direction on Strength of Lattice Structure," *Manufacturing Technology,* vol. 19, no. 6, pp. 947-951, 2019.

[48] J. Zhao, R. Liu, J. Cai, E. Estakhrianhaghighi, A. P. Sasmito, J. Hou and A. Akbarzadeh, "Enhanced Mechanical Properties of Lattice Structures Enabled by Tailoring Oblique Truss Orientation Angle," *Advanced Engineering Materials,* vol. 26, no. 6, p. 2301646, 2024.

[49] X. Gao, M. Fraulob and G. Haïat, "Biomechanical behaviours of the bone–implant interface: a review," *Journal of the Royal Society Interface,* vol. 16, no. 156, 2019.

[50] J. D. Currey, Bones: Structure and Mechanics, Princeton: Princeton University Press, 2022.

[51] D. Sumner, "Long-term implant fixation and stress-shielding in total hip replacement," *Journal of Biomecahnics,* vol. 48, no. 5, pp. 797-800, 2015.

[52] J. Li, P. Habibovio, M. v. d. Doel, C. Wilson, J. d. Wijn, C. v. Blitterswijk and K. d. Groot, "Bone ingrowth in porous titanium implants produced by 3D fiber deposition," *Biomaterials,* vol. 28, no. 18, pp. 2810-2820, 2007.

[53] J. V. d. Stok, O. P. V. D. Jagt, S. Yavari, M. D. Haas, J. Waarsing, H. Jahr, E. V. Lieshout, P. Patka, J. Verhaar, A. Zadpoor and H. Weinans, "Selective laser melting-produced porous titanium scaffolds regenerate bone in critical size cortical bone defects," *Journal of Orthopaedic Research,* vol. 31, no. 5, pp. 792-799, 2013.
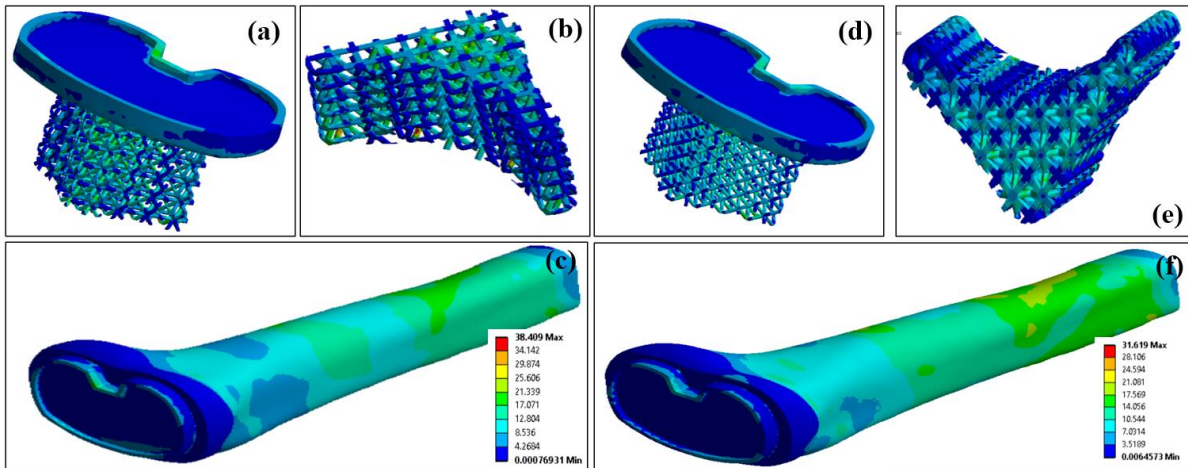
Supplementary Information

Figure. A 1. Level bending equivalent stress distribution of (a) tibia bone implant with FCC lattice, (b) isolated FCC lattice, (c) complete bone with internal FCC lattice, (d) tibia bone with FBCC lattice, (e) isolated FBCC lattice and (f) complete bone with implant with FBCC lattices
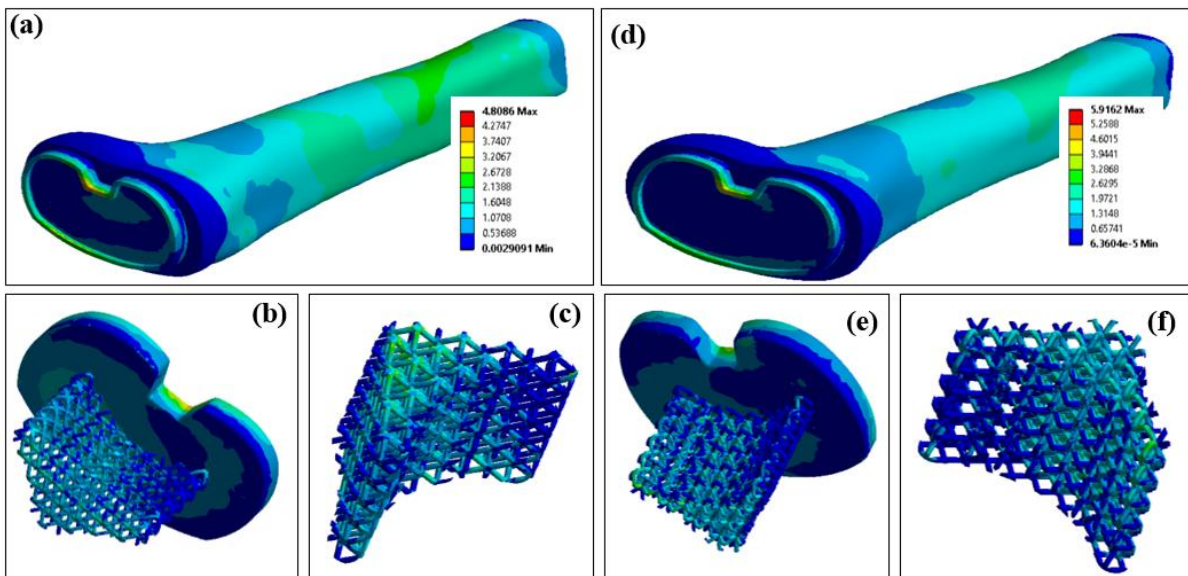

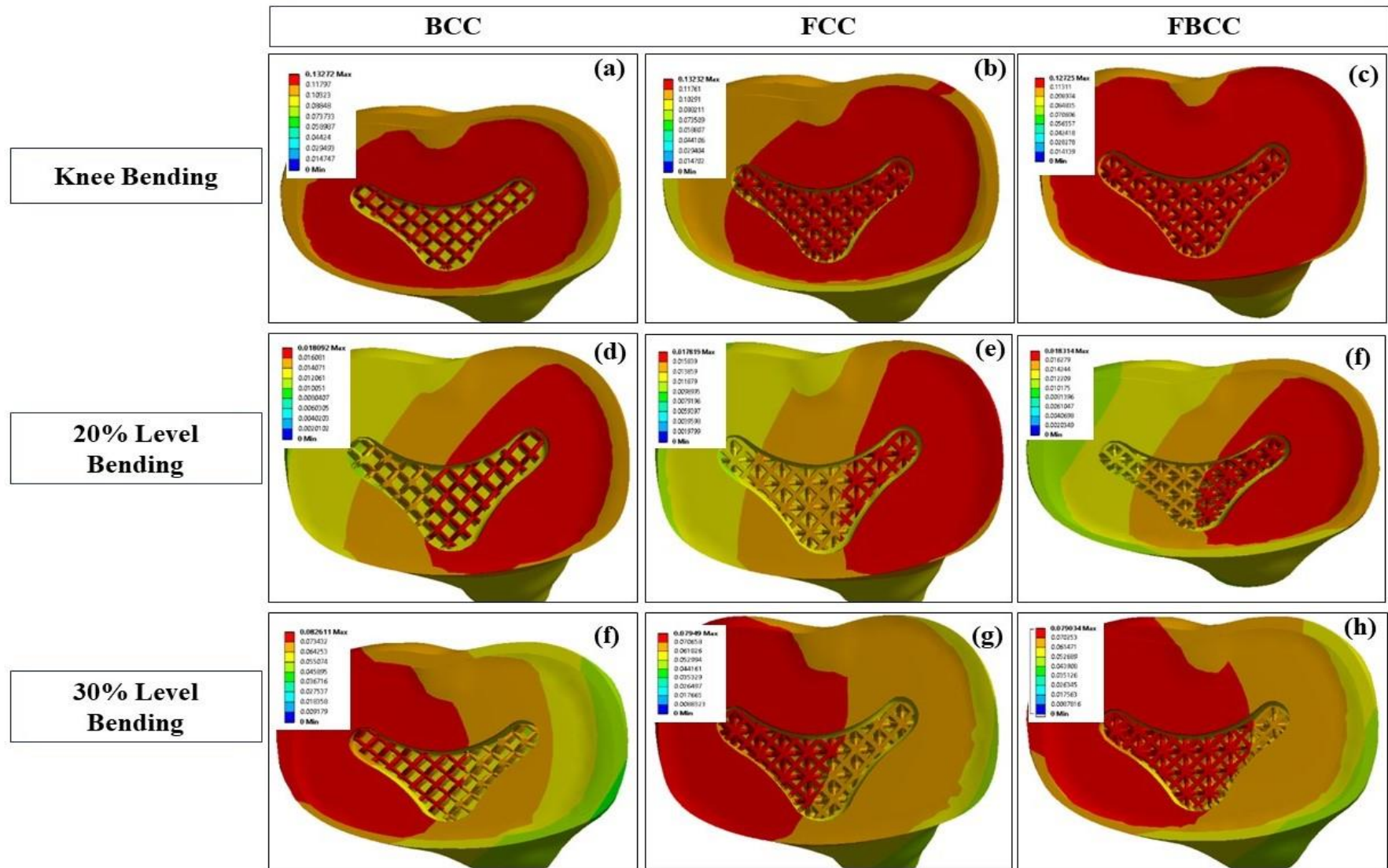**Figure. A 2. 20% level walking effects on equivalent stress of (a, b & c) BCC and (d, e & f) FCC.**

Figure. A 3. Total deformation of all the lattices